An Optimal Control Method for Photovoltaic Grid-Tied-Interleaved Flyback Microinverters to Achieve High Efficiency in Wide Load Range

Zhiliang Zhang, *Member, IEEE*, Xiao-Fei He, and Yan-Fei Liu, *Fellow, IEEE*

***Abstract*—Boundary conduction mode (BCM) and discontinuous conduction mode (DCM) control strategies are widely used for the flyback microinverter. The BCM and DCM control strategies are investigated for the interleaved flyback microinverter concentrating on the loss analysis under different load conditions. These two control strategies have different impact on the loss distribution and thus the efficiency of the flyback microinverter. For the interleaved flyback microinverter, the dominant losses with heavy load include the conduction loss of the power MOSFETs and diodes, and the loss of the transformer; while the dominant losses with light load include the gate driving loss, the turn-off loss of the power MOSFETs and the transformer core loss. Based on the loss analysis, a new hybrid control strategy combing the two-phase DCM and one-phase DCM control is proposed to improve the efficiency in wide load range by reducing the dominant losses depending on the load current. The optimal design method based on the boundary condition of the hybrid control is also presented. The experimental results verify the benefits of the proposed control.**

***Index Terms*—AC module, grid-connected, interleaved flyback, microinverter, photovoltaic (PV).**

I. Introduction

THE interest in exploring renewable energies has grown in the last years due to the energy crisis. Photovoltaic (PV) sources are predicted to have the highest increase 30% in the next decade and to be the biggest contributor on the electricity generation in 2040 [1]. A PV ac module, which is also called the microinverter, is becoming more and more popular and the power range is normally up to about 200 W. Compared to the conventional centralized, string and multistring inverter, the microinverter has many advantages such as higher maximum power point tracking (MPPT) efficiency and lower manufacturing cost through mass production, as well as safe and simple installation [2].

With the rapid development of the market, a lot of research work has been done with the topologies and control methods of the microinverters. The topologies of the single-phase grid-connected PV inverters were reviewed in [3] and [4]. Normally, a boost stage is used to boost the low voltage source provided by the PV panel. An ac module based on dc bus was presented in [5]. A modulated boost stage is used to generate a rectified sinusoidal waveform and a current source inverter (CSI) is used to unfold the rectified waveform into the grid in [6]–[9]. These topologies usually achieve high efficiency under heavy load, but low efficiency under light load (no more than 90% as reported). Moreover, the complexity and additional components of the previous topologies also result in high cost and low power density as a PV ac module.

Alternatively, the microinverter derived from the flyback converter, named as the flyback inverter, is widely used due to its simple structure, lower cost, and higher efficiency [10]. A flyback dc/dc converter with high frequency isolation along with a H-Bridge pulse width modulation (PWM) inverter offers a simple two-stage approach in [11]. A high dc bus voltage allows for the low decoupling capacitance. But both stages operate at high frequency, the total losses are relatively high. A single-stage flyback inverter with the center-tapped secondary winding was presented in [12]–[15]. Each of the secondary winding transfers the energy to the ac side during a half-line period with two additional MOSFETs. A modulated flyback dc/dc converter followed by a CSI was presented in [16] and [17]. The SCRs are used in the unfolding stage to reduce the cost and conduction loss. To further improve the efficiency, a soft-switching-interleaved flyback microinverter under boundary conduction mode (BCM) was presented in [18]. Active clamp and synchronous rectifier technology were adopted in [19]–[21]. But additional auxiliary circuit components are required and this results in higher cost, lower power density, and complex control as a PV ac module. A multiphase-interleaved flyback microinverter with the hybrid control scheme including the interleaved mode and quasiresonant mode is proposed by Enphase Technology [22]. But either a simple flyback mode or an interleaved flyback mode is applied during a half-line period depending on the output power of the PV panel, which limits the further improvement of the efficiency.

A dual-mode switching strategy for the center-tapped secondary winding flyback inverter was presented in [23]. The BCM and discontinuous conduction mode (DCM) modulations

Manuscript received August 15, 2012; revised October 8, 2012 and December 15, 2012; accepted January 31, 2013. Date of current version May 3, 2013. This work was supported by the Priority Academic Program Development of Jiangsu Higher Education Institutions and Public Research Funding from the Jiangsu Key Laboratory of New Energy Generation and Power Conversion. Recommended for publication by Associate Editor J. A. Cobos.

Z. Zhang and X.-F. He are with the Jiangsu Key Laboratory of New Energy Generation and Power Conversion, Nanjing University of Aeronautics and Astronautics, Nanjing 210016, China (e-mail: zlzhang@nuaa.edu.cn; giftxiaofei@nuaa.edu.cn).

Y.-F. Liu is with the Department of Electrical and Computer Engineering, Queen's University, Kingston, ON K7L 3N6, Canada(e-mail: yanfei.liu@queensu.ca).

Color versions of one or more of the figures in this paper are available online at http://ieeexplore.ieee.org.

Digital Object Identifier 10.1109/TPEL.2013.2245919

were used simultaneously during a half-line period, because BCM is more suitable to high-power levels and DCM is better for low-power levels as far as the efficiency is concerned. Owing to the combined control strategy, higher efficiency can be achieved over the conventional BCM control method without additional cost. The reference signal design with the similar control strategy for the single flyback converter with a CSI was proposed in [24]. However, the optimal boundary point between the BCM and DCM are applied to is not clarified regarding to the interleaved microinverters. The two phase inverters are modulated with the same control strategy during the half-line period, and this limits the efficiency improvement within wide load condition. More importantly, the boundary condition of the hybrid control with BCM and DCM is not analyzed, which is so important to design the power stage and the controller for the optimization of the overall performance.

In this paper, the BCM and DCM control strategies are investigated of the interleaved flyback microinverter concentrating on the loss analysis under different load conditions, respectively. It is noted that the DCM control strategy achieves higher efficiency over BCM for the application of the interleaved flyback microinverter within the power range of 200 W. The advantages of two-phase DCM operation are the current sharing and the reduction of the current stress between two interleaved phases so that the conduction loss and turn-off loss of the power MOSFETs and diodes as well as the copper loss of the transformer can be reduced with higher output power. On the other hand, the advantage of one-phase DCM operation is the reduction of the transformer core loss, the driving loss of the power MOSFETs with lower output power. Since the output power is a pulsating power following a squared sine wave, the idea here is to combine two-phase DCM modulation and one-phase DCM modulation simultaneously according to different output power during a half-line period so that the dominant losses can be optimized and high efficiency is achieved in wide load range. In addition, the proposed control method is compatible with the digital implementation and requires no additional auxiliary circuitry.

Section II presents the analysis of the interleaved flyback microinverter under BCM and DCM. Section III presents the proposed control method and its principle of operation. Section IV presents the hardware and software design. The simulation results are also provided in Section V. Section VI contains the experimental results and discussion. Section VII provides a brief conclusion.

II. Analysis of Flyback Inverter Under BCM and DCM

A. Topology of the Interleaved Flyback Microinverter

Fig. 1 shows the main circuit of the interleaved flyback inverter. The inverter comprises of two-phase-interleaved flyback converters and a CSI. S_1 and S_2 are the main power switches; D_1 and D_2 are the rectifier diodes; N_{P1} and N_{P2} are the primary windings, and N_{S1} and N_{S2} are the secondary windings. $S_3 - S_6$ form the CSI to unfold the rectified sinusoidal waveform into the grid. S_3 and S_6 turn ON during the positive-half grid period, while S_4 and S_5 turn ON during the negative-half grid period.

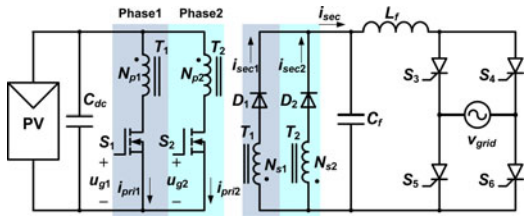

Fig. 1. Interleaved flyback inverter.

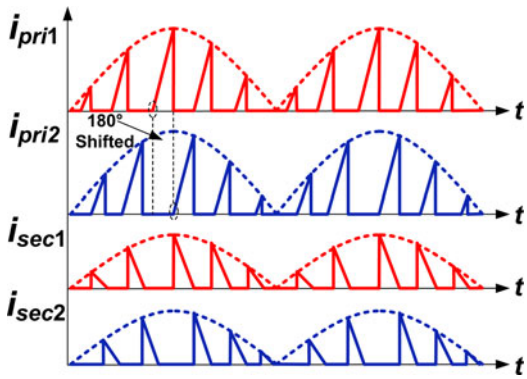

Fig. 2. Current waveforms of the interleaved flyback inverter.

Fig. 2 shows the current waveforms of the interleaved flyback inverter. Each phase is 180° phase shifted in one switching period to achieve ripple cancelation. Thus, a lower output filter inductance can be used.

B. Comparison of BCM and DCM

Fig. 3 shows key waveforms of the interleaved flyback microinverter under BCM and DCM, respectively. Under DCM, a constant switching frequency control is applied. A variable switching frequency is applied under BCM to achieve a sinusoidal output current waveform. It is noticed that the output current frequency is twice of the switching frequency, which leads to the output filter inductance reduction and higher power density can be achieved.

The dominant losses with heavy load include the conduction loss of the MOSFETs and diodes, and the core loss and copper loss of the transformer, while the dominant losses with light load include the driving loss, turn-off loss of the MOSFETs and the transformer core loss. The range of the switching frequency increases dramatically as the power level decreases for the flyback microinverter under BCM. For the microinverter with two phases, the switching frequency range varies from 113 to 480 KHz under BCM at the power level of 200 W [23]. This causes the driving loss and turn-off of the MOSFETs to increase significantly. Therefore, the efficiency under BCM is much lower than DCM under the light-load condition. Table I shows the loss distribution comparison under BCM and DCM under the half-load condition. The specifications are as follows: input voltage: $V_{\rm dc}$ = 36–60 V; grid voltage: V_g = 220 $V_{\rm AC}$; grid frequency: $f_{\rm grid}$ = 50 Hz; switching frequency: f_s = 100 kHz. The

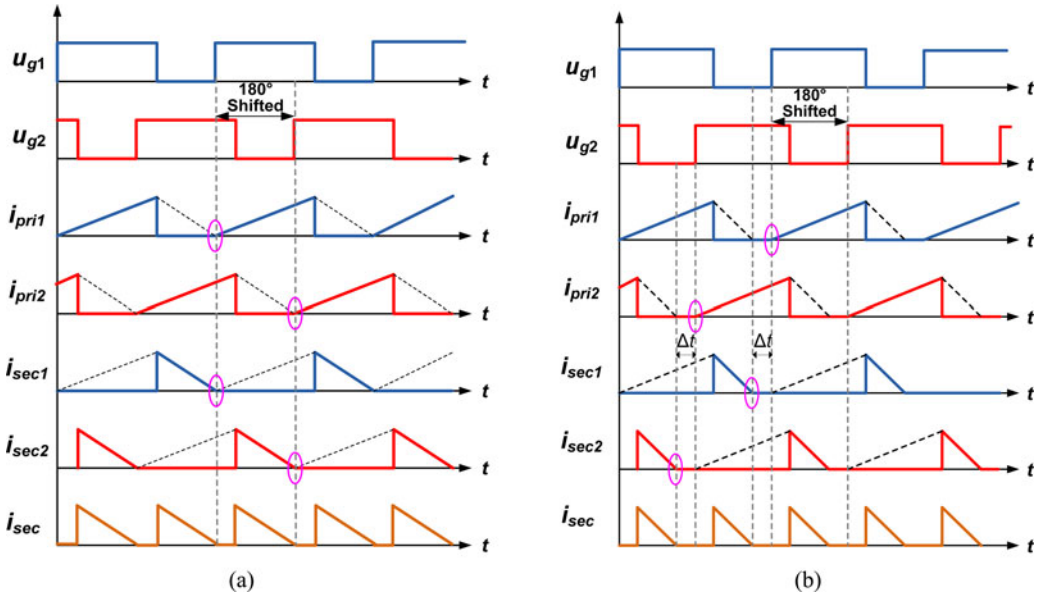

Fig. 3. Key waveforms of the interleaved flyback inverter under BCM and DCM. (a) BCM. (b) DCM.

TABLE I
ESTIMATED LOSS DISTRIBUTION UNDER BCM AND DC FOR THE MICROINVERTER WITH TWO-PHASE OPERATION

	DCM		BCM	
	Loss	Percentage	Loss	Percentage
P_{off}	**0.80 W**	18.3%	**2.50 W**	31.5%
P_{drive}	**0.83 W**	18.9%	**2.83 W**	35.7%
P_{mos}	0.60 W	13.7%	0.40 W	5.04%
P_{core}	**0.84 W**	19.2%	0.99 W	12.5%
P_{cu}	0.71 W	16.2%	0.89 W	11.2%
P_{diode}	0.60 W	13.7%	0.32 W	4.04%

components of the power train are as follows: the transformer: $L_p = 28\ \mu$H, $L_s = 112\ \mu$H; S_1 and S_2: SPW52N50C3 (560 V/52 A from Infineon); D_1 and D_2: IDP12E120 (1200 V/12 A from Infineon); S_3–S_6: S8016N (800 V/16 A from Teccor). The detailed design procedure is provided in Section IV. In this paper, the loss analysis is based on the previous specifications.

Fig. 4 shows the calculated efficiency of the interleaved flyback microinverter under DCM and BCM, respectively. It is noted that the turn-off loss $P_{\rm off}$ and the gate driving loss $P_{\rm drive}$ under BCM are much higher than DCM. This translates into a significant reduction of the light load efficiency.

A comparison of the microinverter under BCM and DCM is shown in Table II. Based on the previous analysis, it should be pointed that for the application of the interleaved flyback microinverter, within the power range of 200 W, DCM has the advantage over BCM. However, it should be noted that even under DCM, the microinverter suffers low efficiency when the load current reduces. Since the peak current control is used under BCM, both primary and secondary current of the transformer need to be sensed. While for the DCM control, the current programmed control is used and only the output current is sensed. The total harmonic distortion (THD) of the DCM operation is 3.79% as illustrated in [24]. Due to the large frequency bandwidth, BCM achieves lower THD as 2.459% in [25]. Since the

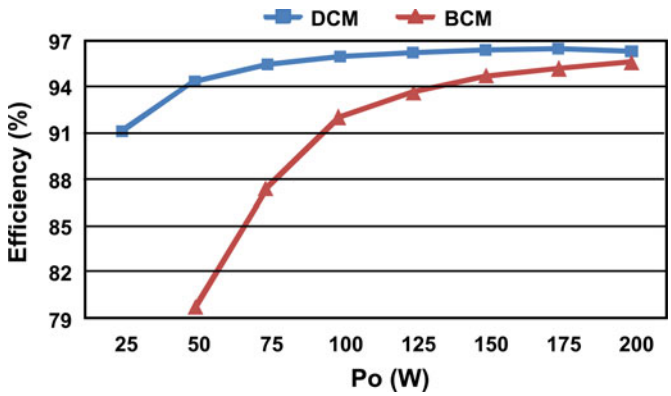

Fig. 4. Calculated efficiency comparison under DCM and BCM for the microinverter with two phase.

TABLE II
COMPARISON OF BCM AND DCM

	BCM	DCM
Switching frequency	VSF	CSF
Power transfer	High	Low
Peak current sensing	Yes	No
Control	Complex	Easy
THD	Low	High
Loss under light load	High	Low

TABLE III
ESTIMATED LOSS DISTRIBUTION OF DCM UNDER DIFFERENT LOAD CONDITIONS FOR THE MICROINVERTER WITH TWO-PHASE OPERATION

	Full load		Quarter load	
	Loss	Percentage	Loss	Percentage
P_{off}	**1.32 W**	**16.8%**	**0.60 W**	**18.2%**
P_{drive}	0.83 W	10.5%	**0.83 W**	**25.2%**
P_{mos}	**1.70 W**	**21.6%**	0.22 W	6.7%
P_{core}	**1.48 W**	**18.8%**	**1.08 W**	**32.7%**
P_{cu}	1.22 W	15.5%	0.27 W	8.1%
P_{diode}	**1.32 W**	**16.8%**	0.30 W	9.1%

proposed control only uses the DCM modulation, the THD of the output current will meet the industrial requirement (<5%) such as IEC 61727.

III. PROPOSED CONTROL METHOD AND PRINCIPLE OF OPERATION

A. Loss Analysis of DCM

Table III shows the calculated loss distribution of a 200-W-interleaved flyback inverter under 100% and 25% load, respectively. It is observed that the dominant losses with heavy load include the conduction loss of the power MOSFETs $P_{\rm mos}$ and diodes $P_{\rm diode}$, the transformer core loss $P_{\rm core}$ and copper loss $P_{\rm cu}$, whereas the dominant losses with light load include the gate driving loss $P_{\rm drive}$, the turn-off loss $P_{\rm off}$ of the power MOSFETs and the transformer core loss $P_{\rm core}$. Therefore, minimizing the dominant losses according to load condition is an effective way to optimize the efficiency in wide load range.

For simplicity, 1Φ DCM represents only one phase operation and 2Φ DCM represents two phases operation under the interleaved mode. On the one hand, the 2Φ DCM operation shares the current and reduces the current stress between two interleaved phases. This is beneficial to reduce the conduction loss and turn-off loss of the power MOSFETs and diodes, as well as the copper loss of the transformer under the heavy-load condition. On the other hand, the 1Φ DCM operation sheds the additional phase of the microinverter, which minimizes the gate driving loss of the power MOSFETs as well as the core loss of the transformer under the light-load condition.

Based on the loss analysis, Fig. 5 shows the efficiency of the interleaved flyback inverter under 1Φ DCM and 2Φ DCM operation. For the sake of the output power, the maximum power transferred by each phase is about 125 W under DCM operation. It is noted that the efficiency improves while operating under 1Φ DCM within the power range of 105 W. Actually, 2Φ DCM and 1Φ DCM can be used simultaneously to modulate the interleaved flyback inverter depending on the load current during a half-line period.

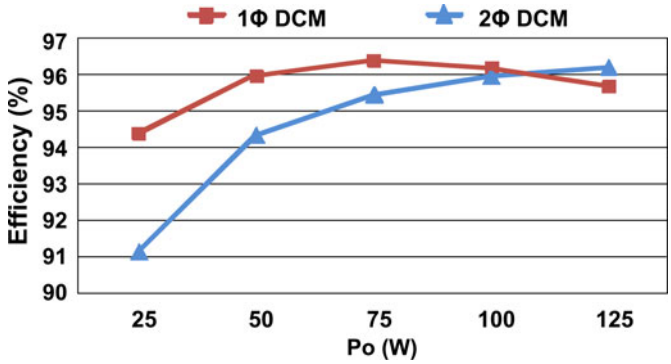

Fig. 5. Calculated efficiency of the interleaved flyback inverter.

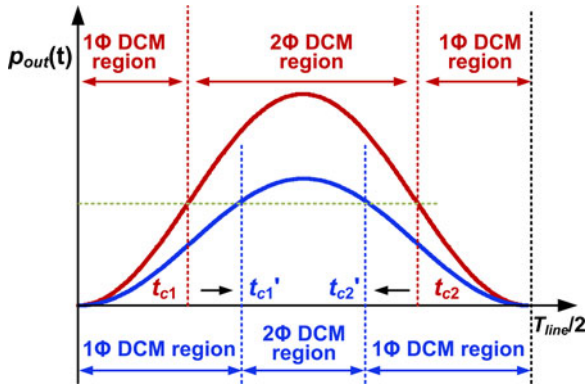

Fig. 6. Output power curve with 1Φ DCM and 2ΦDCM for the interleaved flyback microinverter.

B. Proposed Hybrid Control Method

From the previous analysis, it is interesting to notice that the advantage of 2Φ DCM operation is current sharing between two phases. The conduction loss and turn-off loss of the power MOSFETs and diodes and the copper loss of the transformer can be reduced when the load current is high. The 1Φ DCM operation reduces the driving loss of the power MOSFETs and the transformer core loss. The conventional DCM control only shuts down one phase when the load reduces to some power level. Actually, during the half-line period, either 2Φ DCM or 1Φ DCM control can be applied. It is noticed that the output power $p_{\rm out}\ (t)$ during a half-line period is a pulsating power following a squared sine wave:

$$p_{\rm out}(t) = 2P_o \sin^2(\omega t) \tag{1}$$

where P_o presents the average value of the output power delivered to the grid.

The idea here is to combine the advantages of 2Φ DCM and 1Φ DCM adaptively to the load current during a half-line period, which is similar to the phase shedding technology [26], [27] so that the efficiency can be optimized in wide load rang. Fig. 6 shows the operating region of 1Φ DCM and 2Φ DCM during a half-line period. In Fig. 6, 2Φ DCM is employed when load current is high and 1Φ DCM is employed when the load current is under a certain level. In this way, the dominant losses are reduced depending on the load current and higher efficiency can be achieved in wide load range. Moreover, the proposed control

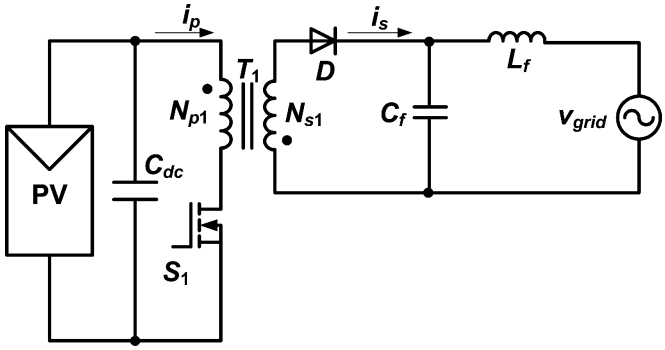

Fig. 7. Equivalent circuit of a single-phase flyback inverter.

is compatible with the digital implementation without additional cost. It should be noted that as P_o decreases, the 2Φ DCM region decreases simultaneously. In particular, when P_o decreases to a certain level, the hybrid modulation merges into only 1Φ DCM. In additional, it should be noted that 2Φ DCM and 1Φ DCM modulations operate simultaneously during a half-line period since the proposed control is based on the instantaneous power delivered to the grid. This clarifies the difference between the hybrid control method proposed in [22].

C. Analysis and Design of Reference Signal for the Proposed Control

For the proposed control method, the reference signal $i_{\rm ref}$ is used to generate the modulated duty cycles and needs to be well designed so that high efficiency and low THD can be achieved. Since the equivalent circuits of the two modules are similar, DCM of a single-phase flyback inverter is analyzed first. Fig. 7 shows the equivalent circuit of the single flyback inverter during a half-line period.

During the S_1 ON time, the primary current i_p increases gradually in a linear relationship with the input voltage $V_{\rm dc}$ and the primary inductance L_p. During the S_1 OFF time, the second current i_s decreases in a linear relationship with the gird voltage $v_g\ (t)$ and the secondary inductance L_s. The turn-on time $T_{\rm on}$ and turn-off time $T_{\rm off}$ in every switching period are

$$T_{\rm on} = \frac{L_p \cdot I_p}{V_{\rm dc}} \tag{2}$$

$$T_{\rm off} = \frac{L_s \cdot I_s}{v_g(t)} \tag{3}$$

where I_p and I_s are the peak value of i_p and i_s in each switching period, respectively. Since I_p equals the reference signal $i_{\rm ref}$, the relationships of I_p and I_s are

$$I_p = i_{\rm ref} \tag{4}$$

$$I_s = I_p \cdot \sqrt{\frac{L_p}{L_s}} = i_{\rm ref} \cdot \sqrt{\frac{L_p}{L_s}}. \tag{5}$$

There is an approximation relationship as (6), where the RMS value of the output current $i_{\rm out}$ equals the average value of i_s in every switching period

$$i_{\rm out} = \frac{I_s \cdot T_{\rm off}}{2T_s}. \tag{6}$$

Considering the previous equations, the relationship between $i_{\rm out}$ and $i_{\rm ref}$ is

$$i_{\rm ref} = \sin(\omega t)\sqrt{\frac{2I_{\rm out} \cdot V_o}{L_p \cdot f_s}} = 2\sin(\omega t)\sqrt{\frac{P_{o1}}{L_p \cdot f_s}} \tag{7}$$

where $I_{\rm out}$ is the peak value of $i_{\rm out}$; V_o is the peak value of $v_g\ (t)$; and P_{o1} is the average output power of each phase. For 2Φ DCM operation, $P_o = 2P_{o1}$. The previous equation can be rewritten as

$$i_{\rm ref} = \sin(\omega t)\sqrt{\frac{2P_o}{L_p \cdot f_s}}. \tag{8}$$

D. Optimal Boundary Condition of 2Φ DCM and 1Φ DCM

For the interleaved flyback microinverter with the proposed control method, the current reference $i_{\rm ref1}$ and $i_{\rm ref2}$ during a half-line period are

$$i_{\rm ref1} = \begin{cases} 2\sin(\omega t)\sqrt{\dfrac{P_o}{L_p \cdot f_s}} & (t < t_{c1}, t > t_{c2}) \\ \sin(\omega t)\sqrt{\dfrac{2P_o}{L_p \cdot f_s}} & (t_{c1} < t < t_{c2}) \end{cases} \tag{9}$$

$$i_{\rm ref2} = \sin(\omega t)\sqrt{\frac{2P_o}{L_p \cdot f_s}} \quad (t_{c1} < t < t_{c2}). \tag{10}$$

Under the light-load condition, 1Φ DCM operation reduces the driving loss of the power MOSFETs and the transformer core loss. As the power level increases, the conduction losses and turn-off loss of power MOSFETs and diodes as well as the loss of the transformer become the dominant losses. 2Φ DCM operation shares the current between two interleaved phases. The idea is to minimize the dominant losses depending on the load condition. As analyzed in Section III, the cross point of the efficiency curves under 2Φ DCM and 1Φ DCM is 105 W as illustrated in Fig. 5. For the convenience of calculation, 100 W is designed as an optimal boundary condition of 1Φ DCM and 2Φ DCM in this case. As a result, t_{c1} and t_{c2} can be obtained from (11) as shown in Fig. 6

$$\sin(\omega t_{c1}) = \sin(\omega t_{c2}) = \sqrt{\frac{200}{4P_o}} = \sqrt{\frac{50}{P_o}}. \tag{11}$$

IV. Design Procedure and Implementation

A. Design Example

Based on the previous analysis, the interleaved flyback inverter of 200 W is presented as a design example and verifies the proposed hybrid control method. The specifications are as follows: input voltage [maximum power point (MPP)]: $V_{\rm dc} =$ 50 V; grid voltage: 220 $V_{\rm AC}$; grid frequency: $f_{\rm grid} = 50$ Hz; switching frequency: $f_s = 100$ kHz; transformer turns ratio:

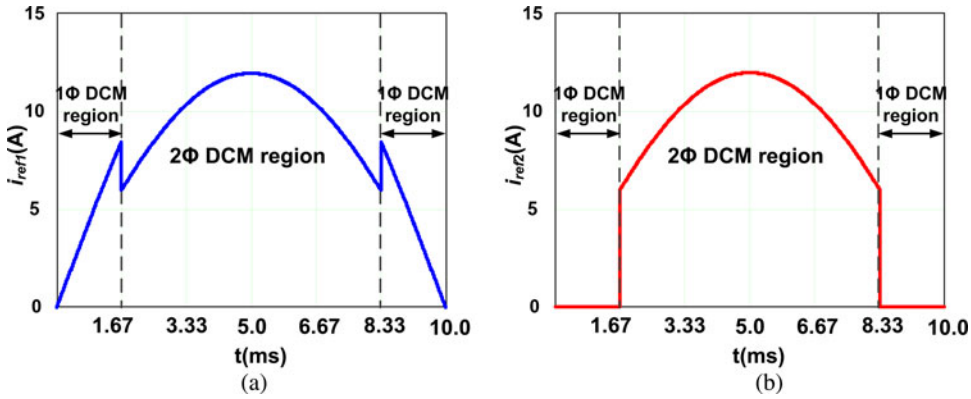

Fig. 8. Reference signals of Phases 1 and 2: full-load condition. (a) Primary current reference signal of Phase 1. (b) Primary current reference signal of Phase 2.

$n = N_p/\mathrm{N_s} = 0.5$. It should be mentioned that the turns ratio has a close relationship with the voltage and current stress of each component. A small turns ratio leads to a higher primary current stress and a higher secondary voltage stress. On the contrary, a larger turns ratio leads to a higher primary voltage stress and a higher secondary current stress.

From (2) and (3), the peak of the primary and secondary current $I_{p,p}$ and $I_{s,p}$ are

$$I_{p,p} = \frac{V_{\mathrm{dc}} T_{\mathrm{onmax}}}{L_p} = \frac{V_{\mathrm{dc}} d_{\max}}{L_p f_s} \tag{12}$$

$$I_{s,p} = \frac{n^2 T_{\mathrm{off}} V_{\mathrm{o}}}{L_p} \tag{13}$$

where $T_{\mathrm{on,max}}$ is the maximum turn-on time, and $d_{\max}$ is the maximum duty cycle.

Combining (5), (12), and (13), the turn-off time T_{off} is

$$T_{\mathrm{off}} = \frac{V_{\mathrm{dc}} d_{\max}}{V_o f_s} = \frac{\lambda d_{\max}}{f_s} = \text{constant} \tag{14}$$

where λ is the ratio of V_{dc}/V_o. For $V_{\mathrm{dc}} = 50$ V and $V_o = 311$ V, λ is 0.161.

In order to reassure that the microinverter will always be under DCM, it has to be confirmed that the T_{off} interval is smaller than the time interval between the switching period and the T_{on} interval

$$T_{\mathrm{off}} \leq \mathrm{T_s} - T_{\mathrm{on,max}}. \tag{15}$$

Combining (12), (14), and (15), the maximum duty cycle $d_{\max}$ is

$$\mathrm{d_{max}} \leq \left(1 + \frac{\lambda}{\mathrm{n}}\right)^{-1}. \tag{16}$$

For $\lambda = 0.161$ and $n = 0.5$, $d_{\max}$ is less than 0.757.

The average of the primary current during a half-line period is

$$I_{p,\mathrm{avg}} = \frac{1}{T_{\mathrm{grid}}/2} \sum_{i=1}^{k} \int_{(i-1)T_s}^{iT_s} i_p(t)dt \tag{17}$$

where

$$\int_{(i-1)T_s}^{iT_s} i_p(t)dt = \int_0^{\mathrm{t_{on}(i-1)}} \frac{V_{\mathrm{dc}} t}{L_p} dt = \frac{V_{\mathrm{dc}}}{2L_p} T_s^2 d_{\max}^2 \sin^2\left(\frac{i\pi}{k}\right). \tag{18}$$

Combining (17) and (18), $I_{p,\mathrm{avg}}$ is

$$\begin{aligned} I_{p,\mathrm{avg}} &= \frac{\mathrm{V_{dc}} T_s^2 d_{\max}^2}{T_{\mathrm{grid}} \mathrm{L_p}} \sum_{i=1}^{k} \sin^2\left(\frac{i\pi}{k}\right) \\ &= \frac{\mathrm{V_{dc}} k T_s^2 d_{\max}^2}{2 T_{\mathrm{grid}} \mathrm{L_p}} = \frac{V_{\mathrm{dc}} T_s d_{\max}^2}{4 L_p}. \end{aligned} \tag{19}$$

The input power is

$$\mathrm{P_{pv}} = 2 V_{\mathrm{dc}} I_{p,\mathrm{avg}} = \frac{V_{\mathrm{dc}}^2 T_s d_{\max}^2}{2 L_p}. \tag{20}$$

For $P_{\mathrm{pv}} = 200$ W, $V_{\mathrm{dc}} = 50$ V, and $d_{\max} = 0.757$, the maximum transformer primary inductance $L_{p\_\max} = 35.79$ μH. With $L_p = 0.8 L_{p\_\max} = 28$ μH, the maximum duty cycle $d_{\max}$ is 0.67.

According to (9), (10), and (11), with the specifications of the interleaved flyback microinverter, the reference signals of the primary and secondary current are

$$i_{\mathrm{ref1}} = \begin{cases} 16.90 \sin(100\pi t) & \left(t < \frac{1}{600},\ t > \frac{1}{120}\right) \\ 11.95 \sin(100\pi t) & \left(\frac{1}{600} < t < \frac{1}{120}\right) \end{cases} \tag{21}$$

$$i_{\mathrm{ref2}} = 11.95 \sin(100\pi t) \quad \left(\frac{1}{600} < t < \frac{1}{120}\right). \tag{22}$$

The waveforms of the reference signals of Phases 1 and 2 for the interleaved flyback microinverter with the proposed control method under the full-load condition are shown in Fig. 8.

With the same design method, the primary current reference signals of Phases 1 and 2 under the half-load and quarter-load conditions can be calculated as illustrated in Figs. 9 and 10. Comparing Figs. 8 and 9, it is observed that as the power level decreases, the 2Φ DCM region decreases simultaneously. When the power level decreases below 50 W, the hybrid modulation with 2Φ DCM and 1Φ DCM merges into only 1Φ DCM region as shown in Fig. 10.

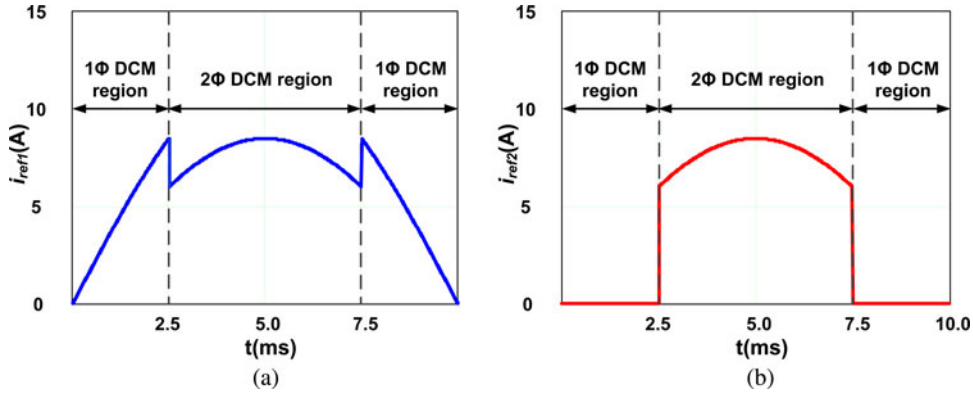

Fig. 9. Reference signals of Phases 1 and 2: half-load condition. (a) Primary current reference signal of Phase 1. (b) Primary current reference signal of Phase 2.

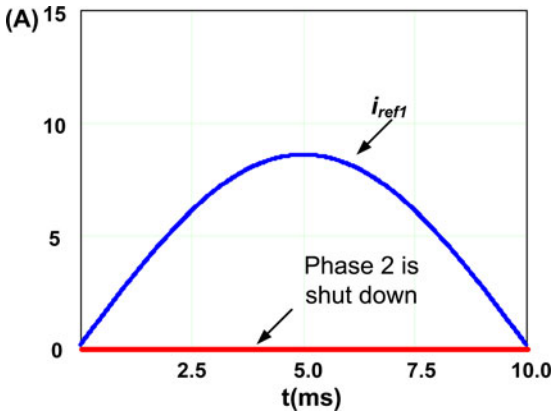

Fig. 10. Reference signals of Phases 1 and 2: quarter-load condition.

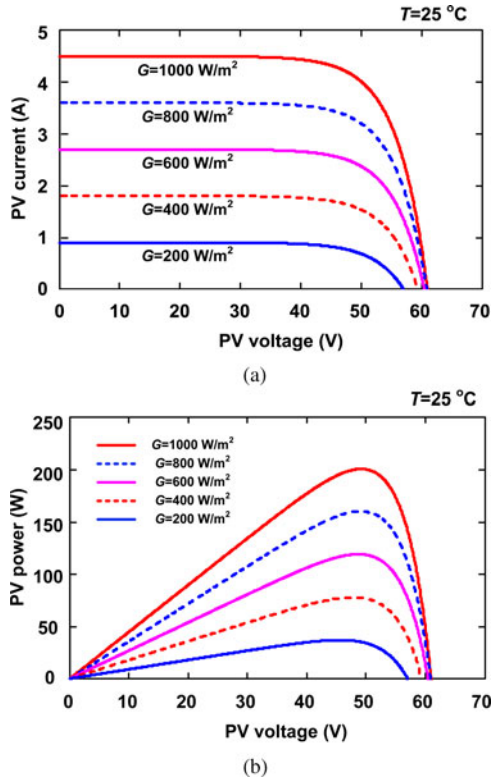

Fig. 11. PV module characteristics for different irradiance levels G. (a) Output current versus voltage. (b) Output power versus voltage.

B. Realization of MPPT

The PV array under uniform irradiance exhibits a current–voltage characteristic with a unique point, called the MPP, where the array produces maximum output power. Fig. 11(a) shows an example of the PV module characteristics in terms of the PV output current versus the voltage. Fig. 11(b) shows the output power versus the current for different irradiance levels G. As noted in Fig. 11, since the $I-V$ characteristic of the PV array, and hence its MPP, changes as a consequence of the variation of the irradiance level, it is necessary to track continuously the MPP in order to maximize the power output from a PV system as far as the PV system efficiency is concerned.

There are many different control algorithms that have been proposed to realize the MPPT, such as the perturb and observe (P&O), the incremental conductance, the fuzzy logic and the neural network, etc. In this paper, the P&O technique is used owing to its simple implementation and low cost.

C. Design of the Input Capacitance

For the single-stage grid-connected microinverter, the MPPT provides the constant output power from the PV panel $P_{\rm pv}$, while the power transferred to the grid $p_{\rm out}\ (t)$ is a pulsating waveform as shown in (1). Generally, the electrolytic capacitor is used to measure the unbalance of the input and output power [28]. When $P_{\rm pv}$ is surplus to $p_{\rm out}\ (t)$, the reminded power is stored into the

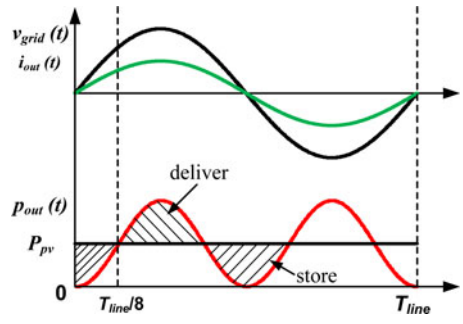

Fig. 12. Input and output waveforms.

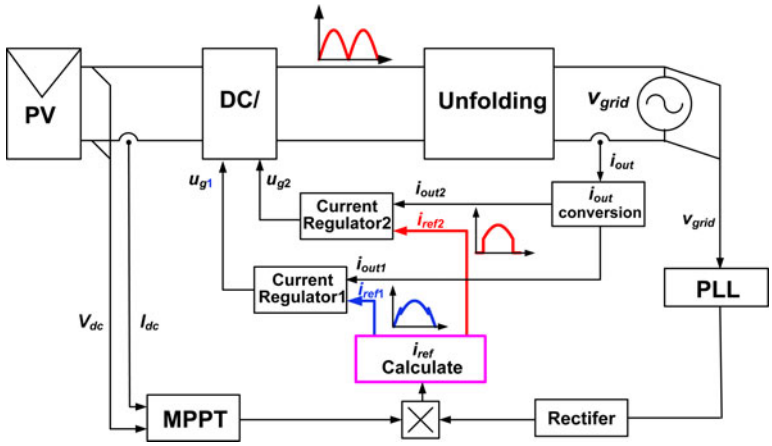

Fig. 13. Control diagram of an interleaved flyback microinverter.

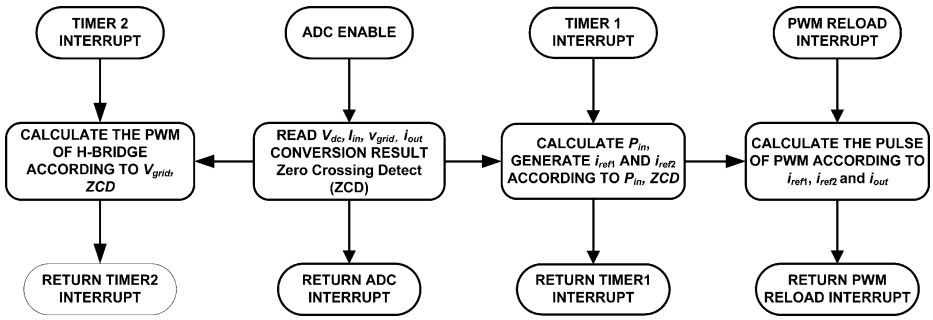

Fig. 14. Program flowchart for control of MC56F8257.

decoupling capacitor. On the contrary, when $P_{\rm pv}$ is smaller than $p_{\rm out}\ (t)$, the decoupling capacitor delivers the power to the output. The input and output waveforms are shown in Fig. 12. The value of the decoupling capacitor is determined by the energy that has to be stored in the capacitor, whose size is

$$C_{\rm dc} = \frac{P_{\rm pv}}{\omega V_{\rm dc} \Delta V} \tag{23}$$

where ω is the angle frequency of the grid voltage, and ΔV is the maximum peak-to-peak ripple voltage of the input capacitor.

For $P_{\rm pv} = 200$ W, $\omega = 2\pi f = 100\pi$, $V_{\rm dc} = 50$ V, and $\Delta V = 2$ V, the required input capacitance is $C_{\rm dc} = 6.37$ mF. Four 1.8-mF electrolytic capacitors are paralleled with lower ESR.

D. Software Design

Fig. 13 shows the control block diagram of the interleaved flyback inverter with the proposed control. The control blocks are implemented by Freescale DSP MC56F8257. In Fig. 13, phase-locked loop is used to detect the phase angle, amplitude, and frequency of the grid voltage. An MPPT block is used to track the MPP of the PV panel.

Fig. 14 shows the program flowchart for the proposed control using the MC56F8257. In the ADC interrupt, $V_{\rm dc}, I_{\rm dc}, v_{\rm grid}$, and $i_{\rm out}$ are sampled. The conversion results are used to achieve the zero-crossing detecting and calculate the input power $P_{\rm pv}$. Timer 1 is used to generate a 20 kHz periodic interrupt, in which the reference signal $i_{\rm ref1}$ and $i_{\rm ref2}$ can be calculated. Then, $i_{\rm ref1}$ and $i_{\rm ref2}$ are sent to the PWM reload interrupt in order to calculate the duty cycle of each phase. At the same time, timer 2 is interrupted at 50 kHz and is used to calculate the PWM waveform for the CSI.

V. Simulation Results and Discussion

A simulation model of the proposed control has been developed. The specifications of the interleaved flyback microinverter are as follows: input voltage $V_{\rm dc} = 36$–60 V; grid voltage $V_{\rm grid} = 220\ V_{\rm ac}$; grid frequency: $f_{\rm grid} = 50$ Hz; switching frequency $f_s = 100$ kHz; gate drive voltage $V_g = 15$ V; primary inductance: $L_P = 28\ \mu$H, and the turns ratio $n = 0.5$.

Fig. 15 shows the key waveforms under the full-load condition. From Fig. 15(a), it is noted that the envelop of the primary current i_{p1} and i_{p2} matches the reference signals as illustrated in Fig. 8. From Fig. 15(b), it is observed that with the interleaved mode, the output current realizes a double switching frequency to realize the ripple cancellation. Figs. 16 and 17 show the key waveforms similar to Fig. 15 under the half-load and quarter-load conditions, respectively. As shown in Figs. 15(a) and 16(b), the 2Φ DCM region decreases simultaneously as the power level decreases. Particularly, as shown in Fig. 17(a), when the power level is much lower, Phase 2 is shut down and only Phase 1 is modulated.

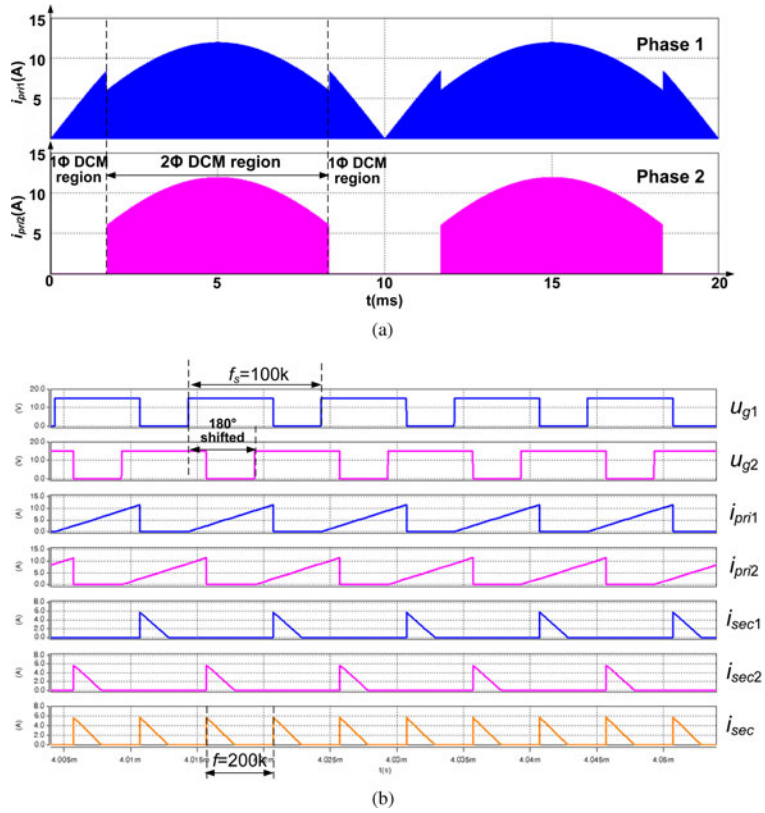

Fig. 15. Key waveforms under the full-load condition. (a) Primary current of Phases 1 and 2. (b) Key waveforms (expanded).

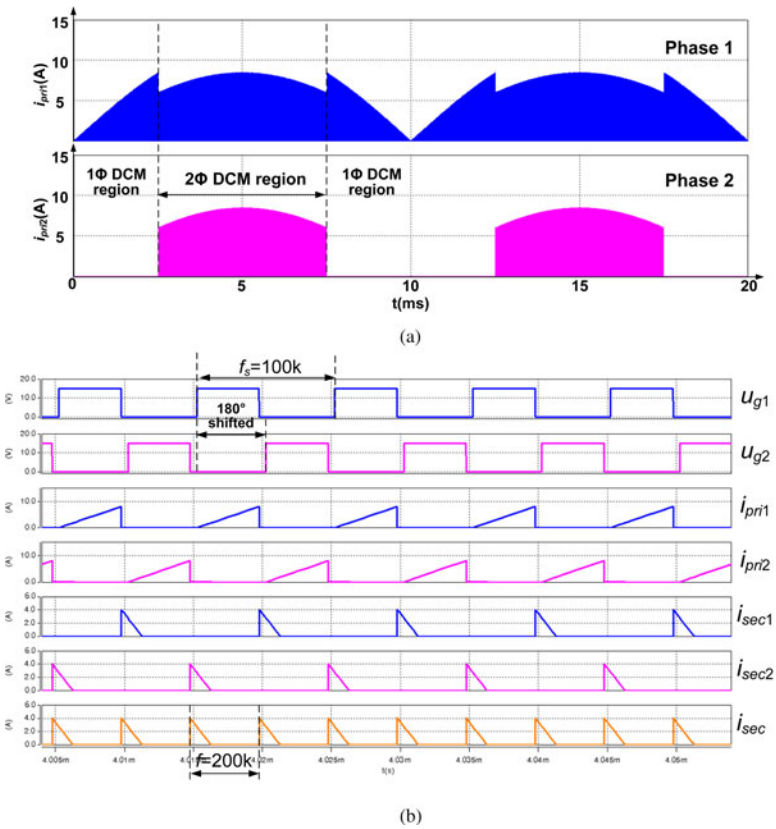

Fig. 16. Key waveforms under the half-load condition. (a) Primary current of Phases 1 and 2. (b) Key waveforms (expanded).

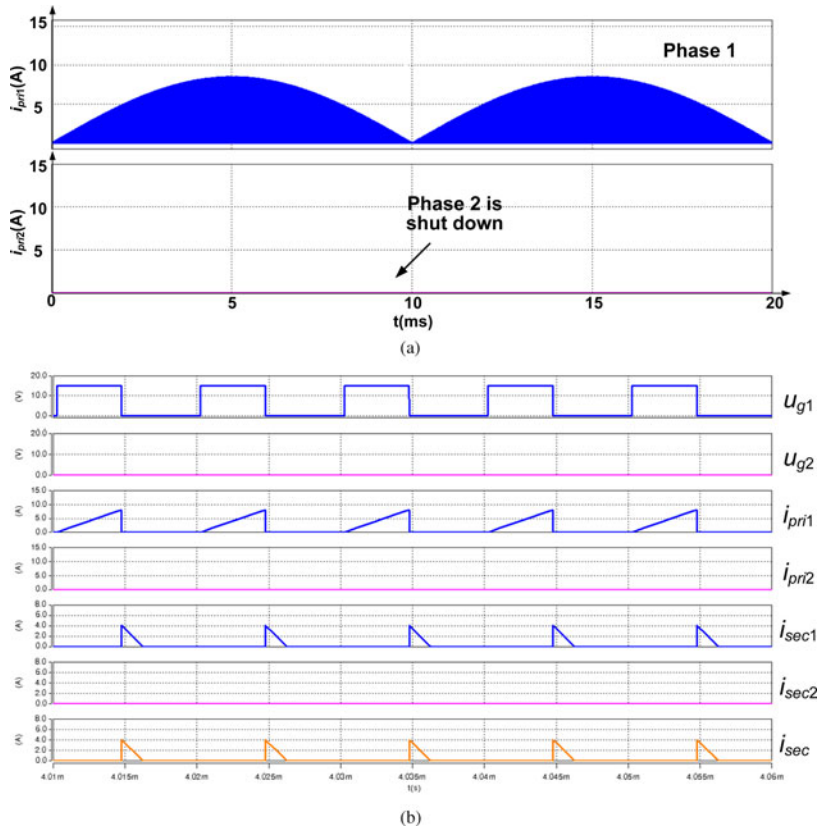

Fig. 17. Key waveforms under the quarter-load condition. (a) Primary current of Phases 1 and 2. (b) Key waveforms (expanded).

VI. Experimental Results and Discussion

To verify the proposed hybrid control method, a prototype of 200 W has been built. The specifications are the same as the analysis in Section V. A PV array simulator is used to verify the MPPT function of the proposed control. The major components used in the circuit are listed as follows: S_1 and S_2: SPW52N50C3; D_1 and D_2: IDP12E120; S_3–S_6: S8016N; the transformer: RM12, $L_P = 28\ \mu$H, $L_s = 112\ \mu$H, $L_k = 0.55\ \mu$H; the output filter inductance: $L_f = 600\ \mu$H; the output filter capacitor: $C_f = 0.33\ \mu$F.

The photograph of a prototype is illustrated in Fig. 18. A hall-effect sensor BJHCS-PS5 is used to sample the input current and an isolation amplifier HCPL-7840 is used to sample the input voltage. Therefore, the input power can be obtained. A hall-effect-based linear current sensor IC ACS712ELCTR-05B-T is used to sense the output current. Two relays are used to achieve grid connection. A Freescale DSP MC56F8257 demo board is used to implement the proposed hybrid control.

Fig. 19 shows the output voltage and current of the PV panel under different conditions. From Fig. 19(a), the PV voltage is 50 V and the current is 4 A under the full-load condition, which translates into the total input power 200 W and matches the MPP as shown in Fig. 11. Under the half-load condition as shown in Fig. 19(b), the PV voltage and current drop to 48 V and 2.1 A, respectively, with the input power of 101 W, which matches the MPP as shown in Fig. 11. Similarly, under the quarter-load condition as shown in Fig. 19(c), it can be observed that the PV voltage and current are 45 V and 1.1 A, respectively, with the input power of 50 W and the MPP is achieved according to Fig. 11.

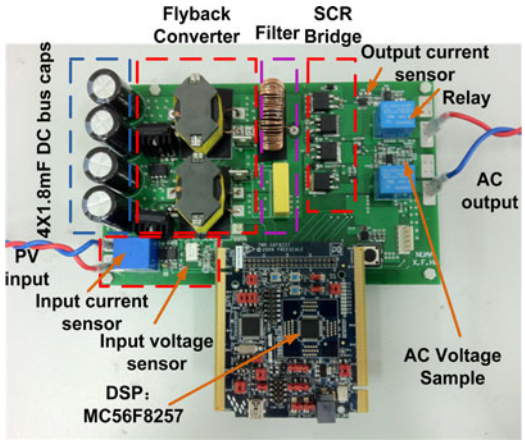

Fig. 18. Photograph of a prototype.

Fig. 20 shows the gate drive voltage and the primary current of Phases 1 and 2 under different load conditions. It is noted that Fig. 20(a), (b), and (c) matches the simulation results in Figs. 15(a), 16(a), and 17(a) regarding the proposed hybrid control method, respectively. It is also observed that as the power level decreases, the 2Φ DCM region decreases accordingly. When the power level decreases below 50 W, the hybrid modulation with 2Φ DCM and 1Φ DCM merges into only 1Φ DCM region as shown in Fig. 20(c). This means the

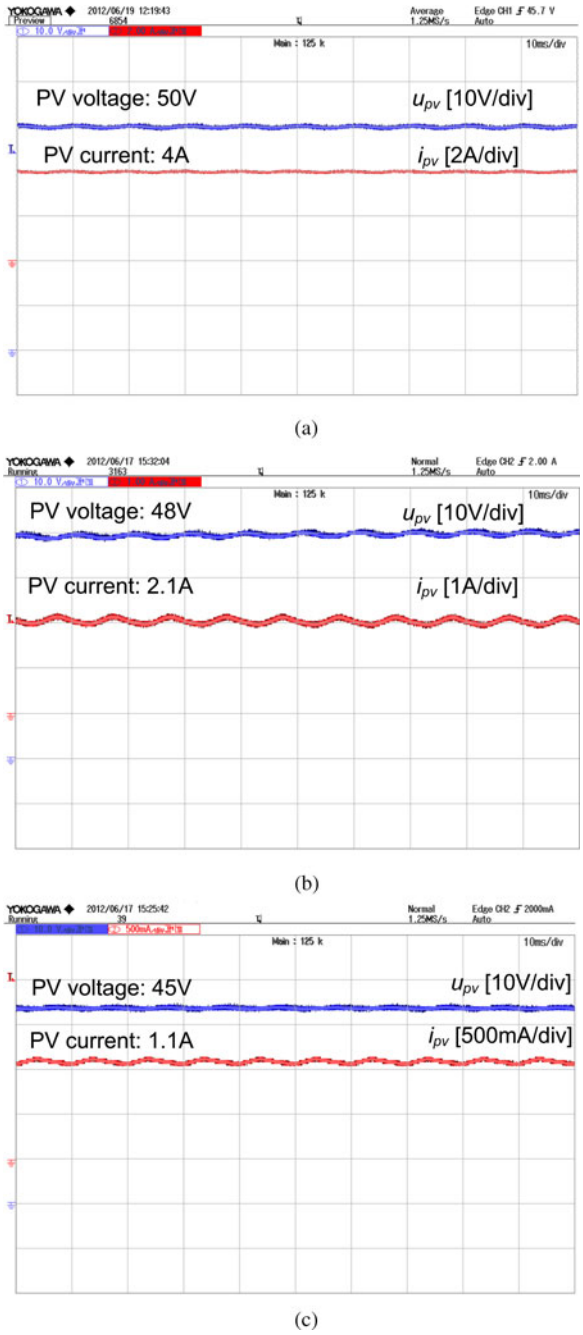

Fig. 19. PV voltage and current under different conditions. (a) Full-load condition. (b) Half-load condition. (c) Quarter-load condition.

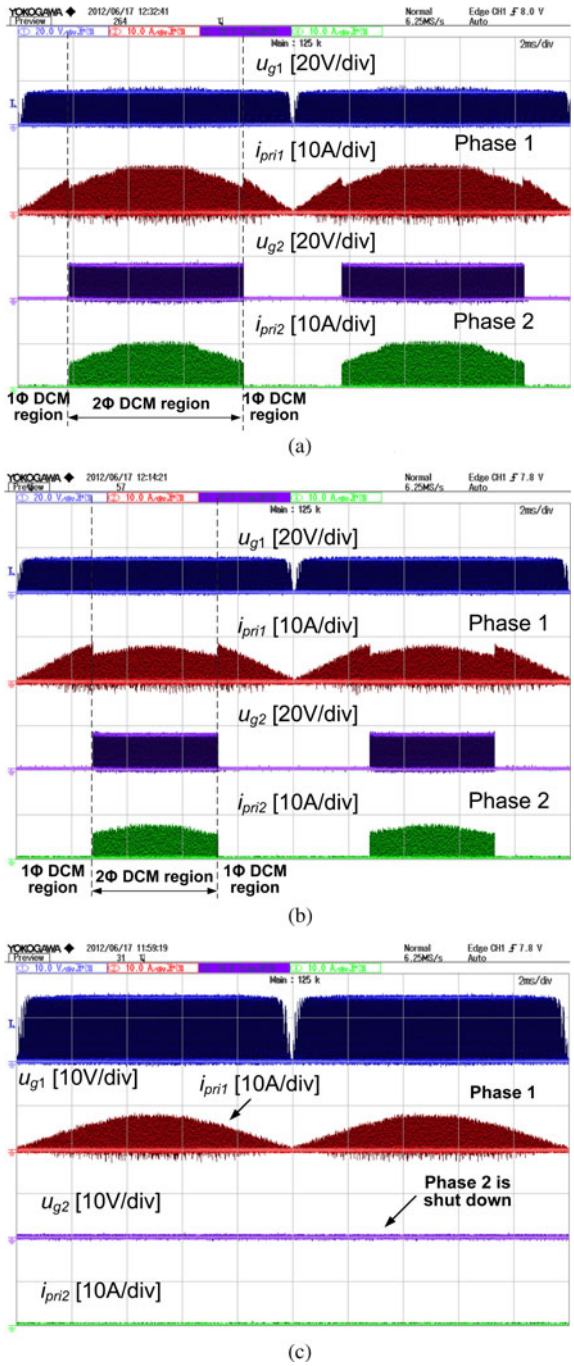

Fig. 20. Gate drive voltage and primary current of Phases 1 and 2 under different conditions. (a) Full-load condition. (b) Half-load condition. (c) Quarter-load condition.

proposed control has the capability to achieve phase-shedding inherently.

Fig. 21 shows the expanded waveforms of the gate drive voltage and the primary current of Phases 1 and 2 under different load conditions. From Fig. 21(a) and (b), the microinverter operates under interleaved mode at 2Φ DCM region. Fig. 21(c) shows that Phase 2 is shut down when the power level decreases below 50 W.

Fig. 22 shows the gird voltage and output current under different load conditions. The output current is able to catch up with the gird voltage with a sinusoidal waveform, and high power factor is achieved under different load conditions.

Fig. 23 shows a transient of MPPT of the PV panel from 35 W (voltage: 42 V, current: 0.8 A) to 76 W (voltage: 47.5 V, current 1.6 A). It is noted that the response to a step PV power is fast and the function of the MPPT has been realized with the proposed control.

Fig. 24 shows the efficiency of the conventional control method and the proposed hybrid control method. In order to do

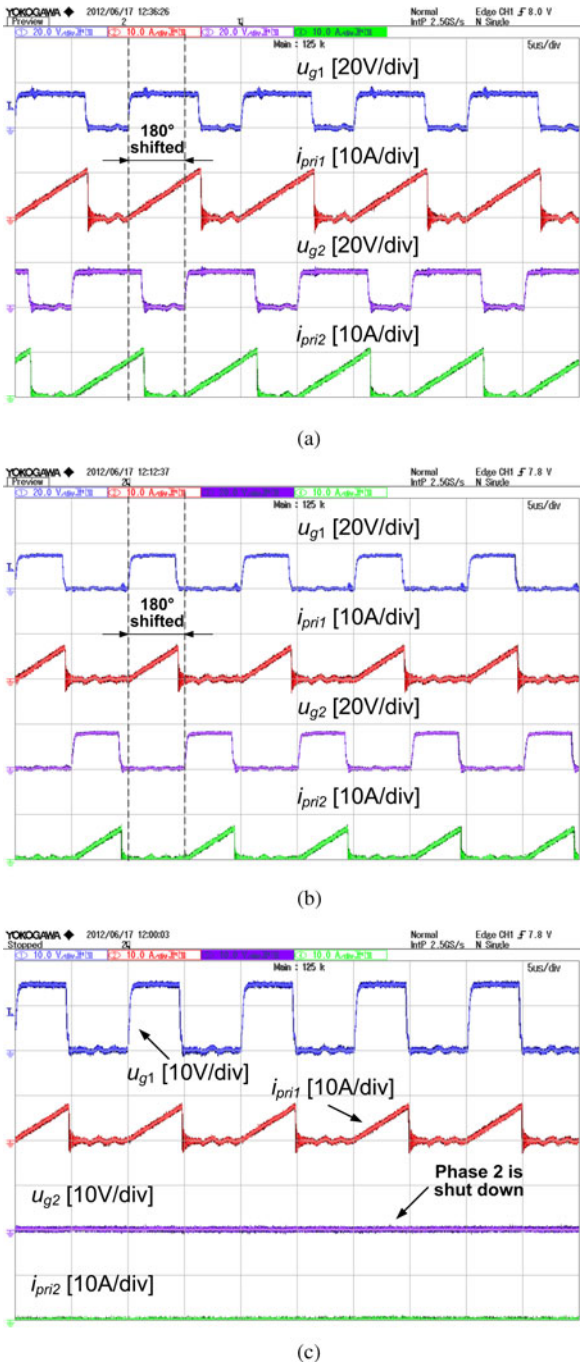

Fig. 21. Gate drive voltage and primary current of Phases 1 and 2 under different conditions (expanded). (a) Full-load condition. (b) Half-load condition. (c) Quarter-load condition.

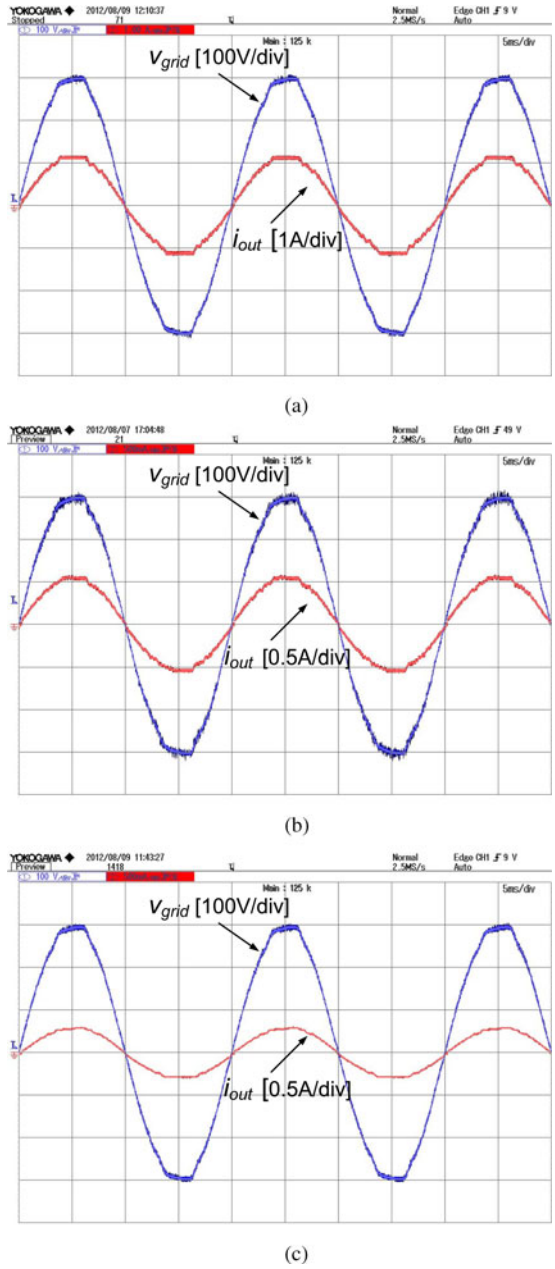

Fig. 22. Grid voltage and output current under different conditions. (a) Full-load condition. (b) Half-load condition. (c) Quarter-load condition.

fair comparison, for the proposed control, the efficiency comparison should be based on the same specifications and the power train components. With light load as P_o is 50 W, the hybrid modulation with 2Φ DCM and 1Φ DCM merges into only 1Φ DCM region. The total loss of the microinverter is reduced by 1.8 W and the efficiency can be improved by 4% over the conventional two-phase-interleaved mode. With heavy load as P_o is 200 W, the 1Φ DCM region reduces and the loss reduction is 1.4 W, which translates into the efficiency improvement of 0.7%.

VII. Conclusion

In this paper, the loss distribution and the efficiency of the interleaved flyback microinverter under BCM and DCM are investigated analytically under different power levels. It is found that DCM is a better choice than BCM within the power range of 200 W. For the interleaved flyback microinverter, the dominant losses with heavy load include the conduction loss of the power MOSFETs and diodes, and the core loss and copper loss of the transformer, while the dominant losses with light load include the gate driving loss, turn-off loss of the power MOSFETs and

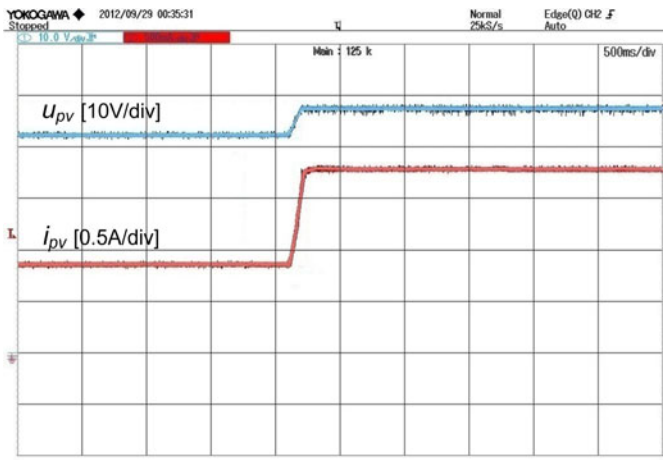

Fig. 23. Response to step PV power.

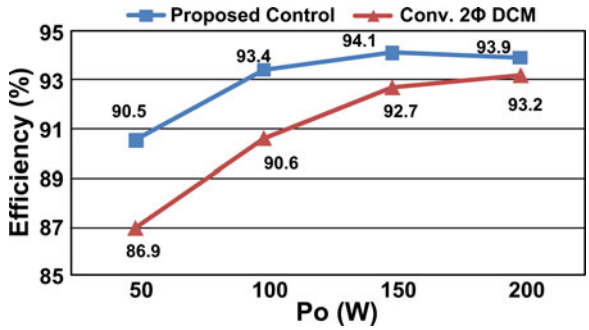

Fig. 24. Efficiency comparison of the conventional control and proposed hybrid control.

the transformer core loss. The 2Φ DCM operation shares the current and reduces the current stress between two interleaved phases. The conduction loss and turn-off loss of the power MOSFETs and diodes and the copper loss of the transformer can be reduced at heavy load, and the 1Φ DCM reduces the driving loss of the main MOSFETs and the core loss of the transformer under the light-load condition. A new hybrid control strategy combining the 2Φ DCM and 1Φ DCM control during a half-line period is proposed. With the proposed control strategy, high efficiency can be achieved in wide load rang by reducing the dominant losses depending on the load current.

The experimental results verified the proposed control with the MPPT function. With the proposed control, the efficiency is improved around 4% under the light-load condition. Even under the heavy-load condition, the efficiency could be improved by 0.7%. Moreover, the proposed control method is compatible with the digital implementation and requires no additional auxiliary circuitry.

REFERENCES

[1] (2004). [Online]. Available: http://www.erec.org/media/publications/2040-scenario.html

[2] W. Yu, C. Hutchens, J. S. Lai, and T. Hegarty, "High efficiency converter with charge pump and coupled inductor for wide input photovoltaic AC module application," in *Proc. IEEE Energy Convers. Congr. Expo.*, 2009, pp. 3895–3900.

[3] S. B. Kjaer, J. K. Pedersen, and F. Blaabjerg, "A review of single-phase grid-connected inverter for photovoltaic modules," *IEEE Trans. Ind. Appl.*, vol. 41, no. 5, pp. 1292–1306, Sep./Oct. 2005.

[4] Q. Li and P. Wolfs, "A review of the single phase photovoltaic module integrated converter topologies with three different DC link configurations," *IEEE Trans. Power Electron.*, vol. 23, no. 3, pp. 1320–1333, May 2008.

[5] L. Zhang, K. Sun, Y. Xing, L. Feng, and H. Ge, "A modular grid-connected photovoltaic generation system based on DC bus," *IEEE Trans. Power Electron.*, vol. 26, no. 2, pp. 523–531, Feb. 2011.

[6] S. Jiang, D. Cao, Y. Li, and F. Z. Peng, "Grid-connected boost-half-bridge photovoltaic microinverter system using repetitive current control and maximum power point tracking," *IEEE Trans. Power Electron.*, vol. 27, no. 11, pp. 4711–4722, Nov. 2012.

[7] Z. Liang, R. Guo, J. Li, and A. Q. Huang, "A high-efficiency PV module-integrated DC/DC converter for PV energy harvest in FREEDM system," *IEEE Trans. Power Electron.*, vol. 26, no. 3, pp. 897–909, Mar. 2011.

[8] C. Prapanavarat, M. Barnes, and N. Jenkins, "Investigation of the performance of a photovoltaic AC module," *IEE Proc. Gener., Trans. Distrib.*, vol. 149, no. 4, pp. 472–478, Jul. 2002.

[9] T. Shimizu and S. Suzuki, "Control of a high efficiency PV inverter with power decouping function," in *Proc. IEEE Int. Conf. Power Electron. ECCE Asia*, 2011, pp. 1533–1539.

[10] N. Kutkut and H. Hu, "Photovoltaic micro-inverter: Topologies, control aspects, reliability issues, and applicable standards," in *Proc. IEEE Energy Convers. Congr. Expo.*, 2010, pp. 5–18.

[11] D. C. Martins and R. Demonti, "Grid connected PV system using two energy processing stages," in *Proc. IEEE Photovoltaic Spec. Conf.*, 2002, pp. 1649–1652.

[12] T. Shimizu, K. Wada, and N. Nakamura, "Flyback type single-phase utility interactive inverter with power pulsation decoupling on the DC input for an AC photovoltaic module system," *IEEE Trans. Power Electron.*, vol. 21, no. 5, pp. 1264–1272, Sep. 2006.

[13] A. C. Kyritsis, E. C. Tatakis, and N. P. Papanikolaou, "Optimum design of the current-source flyback inverter for decentralized grid-connected photovoltaic systems," *IEEE Trans. Energy Convers.*, vol. 23, no. 1, pp. 281–293, Mar. 2008.

[14] A. C. Nanakos, E. C. Tatakis, and N. P. Papanikolaou, "A weighted-efficiency-oriented design methodology of flyback inverter for AC photovoltaic modules," *IEEE Trans. Power Electron.*, vol. 27, no. 7, pp. 3221–3233, Jul. 2012.

[15] Y. Li and R. Oruganti, "A low cost flyback CCM inverter for AC module application," *IEEE Trans. Power Electron.*, vol. 27, no. 3, pp. 1295–1303, Mar. 2012.

[16] S. Mekhilef, N. A. Rahim, and A. M. Omar, "A new solar energy conversion scheme implemented using grid-tied single phase inverter," in *Proc. IEEE TENCON*, 2000, pp. 524–527.

[17] E. Achille, T. Martiré, C. Glaize, and C. Joubert, "Optimized DC–AC boost converters for modular photovoltaic grid-connected generators," in *Proc. IEEE Int. Symp. Ind. Electron.*, 2004, pp. 1005–1010.

[18] J. Y. Gu, H. F. Wu, G. C. Chen, and Y. Xing, "Research on photovoltaic grid-connected inverter based on soft-switching interleaved flyback converter," in *Proc. IEEE Conf. Ind. Electron. Appl.*, 2010, pp. 1209–1214.

[19] Q. Mo, M. Chen, Z. Zhang, Y. Zhang, and Z. Qian, "Digitally controlled active clamp interleaved flyback converters for improving efficiency in photovoltaic grid-connected micro-inverter," in *Proc. IEEE Appl. Power Electron. Conf. Expo.*, 2012, pp. 555–562.

[20] Y. H. Kim, J. G. Kim, C. Y. Won, Y. C. Jung, and T. W. Lee, "Soft switching interleaved active clamp flyback inverter for a photovaltaic AC module system," in *Proc. Eur. Conf. Power Electron. Appl.*, 2011, pp. 1–9.

[21] D. K. Ryu, Y. H. Kim, J. G. Kim, C. Y. Won, and Y. C. Jung, "Interleaved active clamp flyback inverter using a synchronous rectifier for a photovoltaic AC module system," in *Proc. IEEE Int. Conf. Power Electron.*, 2011, pp. 2631–2636.

[22] M. Fornage, "Method and apparatus for converting direct current to alternating current," U. S. Patent US7796412B2, Sep. 14, 2010..

[23] Y. H. Ji, D. Y. Jung, J. H. Kim, C. Y. Won, and D. S. Oh, "Dual mode switching strategy of flyback inverter for photovoltaic AC modules," in *Proc. IEEE Int. Power Electron. Conf.*, 2010, pp. 2924–2929.

[24] Z. Zhang, M. Chen, M. Gao, Q. Mo, and Z. Qian, "An optimal control method for grid-connected photovoltaic micro-inverter to improve the efficiency at light-load condition," in *Proc. IEEE Energy Convers. Congr. Expo.*, 2011, pp. 219–224.

[25] M. Gao, M. Chen, Q. Mo, Z. Qian, and Y. Luo, "Research on output current of interleaved flyback in boundary conduction mode for photovoltaic AC module application," in *Proc. IEEE Energy Convers. Congr. Expo.*, 2011, pp. 770–775.

[26] W. H. Chang, Y. C. Lin, and D. Chen, "Operation phase number dependent compensation of a multi-phase buck converter," U.S. Patent US20110084673A1, Apr. 15, 2011.
[27] A. Costabeber, P. Mattavelli, and S. Saggini, "Digital time-optimal phase shedding in multiphase buck converters," *IEEE Trans. Power Electron. Lett.*, vol. 25, no. 9, pp. 2242–2247, Sep. 2010.
[28] D. Li, Z. Zhang, B. Xu, M. Chen, and Z. Qian, "A method of power decoupling for long life micro-inverter," in *Proc. 37th Annu. Conf. IEEE Ind. Electron. Soc.*, 2011, pp. 802–807.

Zhiliang Zhang (S'03–M'09) received the B.Sc. and M.Sc. degrees in electrical and automation engineering from the Nanjing University of Aeronautics and Astronautics (NUAA), Nanjing, China, in 2002 and 2005, respectively, and the Ph.D. degree from the Department of Electrical and Computer Engineering, Queen's University, Kingston, ON, Canada, in 2009.

Since June 2009, he has been an Associate Professor with the Aero-Power Sci-Tech Center, NUAA. He was a Design Engineering Intern from June to September, 2007 at the Burlington Design Center, VT, Linear Technology Corporation. He received the Graduate Scholarship through Lite-On Technology Corporation in 2004. He is a winner of "United Technologies Corporation Rong Hong Endowment" in 1999. His research interests include high-frequency dc–dc converters, power integrated circuit, digital control techniques for power electronics and renewable energy conversion system.

Xiao-Fei He received the B.S. degree in electrical engineering from the Nanjing University of Aeronautics and Astronautics, Nanjing, China, in 2011, where he is currently working toward the M.S. degree at the Aero-Power Sci-Tech Center.

His research interests include power electronics for the renewable energy system and battery energy storage system.

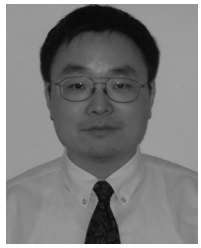

Yan-Fei Liu (M'94–SM'97–F'13) received the B.Sc. and M.Sc. degrees from the Department of Electrical Engineering, Zhejiang University, Hangzhou, China, in 1984 and 1987, respectively, and the Ph.D. degree from the Department of Electrical and Computer Engineering, Queen's University, Kingston, ON, Canada, in 1994.

He is currently a Professor in the Department of Electrical and Computer Engineering, Queen's University. From February 1994 to July 1999, he was a Technical Advisor with the Advanced Power System division of Astec (formerly Nortel Networks), where he was responsible for high-quality design, new products, and technology development. His research interests include digital control technologies for the dc–dc switching converter and ac–dc converter with power factor correction, current source MOSFET drive technology, topologies and control for voltage regulator application, electromagnetic interference filter design methodologies for switching converters, topologies and controls for high switching frequency, low switching loss converters, modeling and analysis of core loss and copper loss for high frequency planar magnetics, large signal modeling of switching converters.

Dr. Liu received the "Premiere's Research Excellent Award" in 2001, Golden Apple Teaching Award in 2000, 2008, and 2009, all in Queen's University, and "1997 Award in Excellence in Technology" in Nortel Networks.